

less than $\sqrt{2}$ in our experiments and will start scaling as $\propto \delta\nu^{-1/2}$ for $\tau \gg \tau_{\text{msd}}$ or $\delta\nu \ll 100$ Hz. To enhance sensitivity, T_{read} can be shortened by increasing the collection efficiency of NV fluorescence photons (29, 30). On the other hand, application of compressed sensing would reduce the overall measurement repetitions needed to reach a certain signal-to-noise ratio (31). Further enhancement can be achieved by incorporating more memory spins (proximal host ^{13}C spins), which would allow the use of quantum algorithms such as quantum Fourier transform or quantum error correction, resulting in measurement speed-up and more robustness (32).

The discrepancy in spectral resolution of the present nanoscale NMR measurement and the measured broad ^1H linewidth can be overcome, for example, in liquid-state NMR by using large sample molecules in nanocapsules such as liposomes, micelles, or polymer shells (33–35). Although the use of large sample molecules may have an impact on molecular structures, they will prevent translational diffusion out of the detection volume and still allow averaging out of the inhomogeneous magnetic field. However, for solid-state NMR the measured linewidth was limited by the finite pulse length in the homonuclear decoupling sequence (36). The use of a cross-polarization power equipment would thus further improve resolution, enabling chemical structure analysis. Additionally, in NV nanoscale NMR experiments, the use of a ^1H lock channel to cause the host ^1C spins can be used to determine the magnetic field very precisely (<0.001 ppm) (23).

This work paves the way for numerous applications of NV nanoscale NMR. For example, sample spin density and T_1 and T_2 of sample spin for chemical shift T_1 and T_2 in cells with nanometer spatial resolution would offer a promising contrast mechanism for op-

REFERENCES AND NOTES

7. W. P. A. de Bartholomé, R. E. J. *Anal. Chem.* **64**, 2226-2246 (1992).
8. H. Ouchikiri et al., *Anal. Sci.* **13**, 374-376 (1998).
9. K. Kikuchi et al., *Anal. Sci.* **14**, 933-935 (1999).
10. P. C. de Laet, *Nature* **342**, 190-195 (1993).
11. E. Goethel, C. Laet, and G. Loh, *Anal. Sci.* **13**, 469-476 (1998).
12. Y. G. Kozlov, V. G. Kozlov, and V. A. Kozlov, *Anal. Sci.* **13**, 1200-1201 (1998).
13. J. H. J. van der Greef, *Anal. Sci.* **14**, 109-112 (1999).
14. C. J. Degen, M. Poggio, H. A. J. Harris, C. J. Remmer, D. Rugar, and J. H. J. van der Greef, *Anal. Sci.* **14**, 103-105 (1999).
15. M. M. Szwarc, et al., *IEEE Trans. on Systems, Man, & Cybernetics* **19**, 757-760 (1989).
16. I. H. Savelle, et al., *Let. Am. J. Sports* **20**, 1022-1024 (1993).
17. S. N. Patel, et al., *Proc. Natl. Acad. Sci. U.S.A.* **93**, 10696-10702 (1996).
18. M. Szwarc, *Proc. Lithuan. Acad. Sci. Appl. Natl. Acad. Phys.* **11**, 22 (1996).
19. H. J. M. Jansen, et al., *Science* **239**, 567-569 (1998).
20. J. T. Staudacher, et al., *Science* **239**, 950-953 (1998).
21. L. H. J. van der Greef, et al., *Anal. Sci.* **14**, 107-109 (1999).
22. T. Hübner, D. Schmidt-Luck, F. Beutler, L. W. Juchacz, and T. Hübner, *Anal. Sci.* **10**, 125-128 (1994).
23. T. Hübner, et al., *Anal. Sci.* **14**, 119-121 (1999).
24. S. J. DeRubeis, et al., *Nat. Neurosci.* **1**, 329-334 (1998).
25. T. J. Staudacher, et al., *Nat. Neurosci.* **6**, 857 (2003).
26. X. Kong, A. Zark, J. Lu, and P. McGuffee, *J. Neurosci.* **22**, 1066-1072 (2002).
27. N. Aslam, et al., *Rev. Sci. Instrum.* **66**, 064704 (1995).

SCIENCE sciencemag.org

22. S. Zaiser et al., *Nat. Commun.* **7**, 12279 (2016).
23. M. Plenier et al., Nonrelativistic quantum memory enables sensor-unlimited nanoscale spectroscopy of finite quantum systems. *arXiv:1605.05675* [quant-ph] (18 October 2016).
24. G. Sabaumariam et al., *Nat. Mater.* **8**, 383–387 (2009).
25. M. P. M. et al., *Phys. Rev. B* **93**, 045425 (2016).
26. F. R. Santos, R. Chaves, M. M. Morton, *J. Polym. Sci. Polym. Lett. Ed.* **11**, 449–452 (1973).
27. Q. Chen, K. Schmidt-Roß, *Solid State Nucl. Magn. Reson.* **29**, 142–155 (2005).
28. A. Abragam, M. Goldman, *Nuclear Magnetism: Order and Disorder* (Oxford Univ. Press, 1962).
29. S. A. Marmorek et al., *Nat. Mater.* **15**, 365–369 (2015).
30. L. Li et al., *Nano Lett.* **15**, 1493–1497 (2015).
31. J. Scheurer et al., *Sci. Rep.* **5**, 17728 (2015).
32. T. Lindén et al., *Phys. Rev. Lett.* **116**, 230502 (2016).
33. B. P. Tirosh et al., *Annu. Rev. Mater. Res.* **41**, 1–20 (2011).

ACKNOWLEDGMENTS

We thank S. Zaiser, N. Alt, and A. Momenzadeh for fruitful discussions and technical advice. We acknowledge I. Jakobi for graphics design. The NMR measurements with the 400-MHz NMR spectrometer were acquired by K. Dirnberger and B. Ormeciarski from the Institute of

Polymer Chemistry, University of Stuttgart. We acknowledge financial support by the German Science Foundation (SFB-TR 22, SPP1503), the EU (DREAMS, SME), the Max Planck Society, the Volkswagen Stiftung, and Japan Science and Technology Agency and Japan Society for the Promotion of Science KAKENHI (nos. 26246001 and 26220903). F.F.O. acknowledges the financial support by Conselho Nacional de Desenvolvimento Científico e Tecnológico (CNPq) project no. 202446/2013-0. Data supporting the findings of this study are available within the article and its supplementary materials and from the corresponding authors upon reasonable request.

SUPPLEMENTARY MATERIALS

www.sciencemag.org/content/357/6346/67/suppl/DC1
Materials and Methods
Supplementary Text

Figs. S1 to S5

Tables S1 to S3
 04 February 2014, 09:00

References (34-48)

1 February 2017: <https://doi.org/10.1175/JCLI-D-16-0202.1>

Published online 1 July 2011
10.1126/science.1207101

SUPERCONDUCTIVITY

Femtosecond electron-phonon lock-in by photoemission and x-ray free-electron laser

S. Gerber,^{1,2,a} S.-L. Yang,^{1,2,b} D. Zhu,⁴ H. Soifer,¹ J. A. Sobota,^{1,5} S. Rebec,^{1,3} J. J. Lee,^{1,3} T. Jia,^{1,3} B. Moritz,⁴ C. Jia,¹ A. Gauthier,^{1,3} Y. Li,⁴ D. Leuenberger,¹ Y. Zhang,⁶ L. Chaix,¹ W. Li,⁴ H. Jang,⁷ J.-S. Lee,⁷ M. Yi,⁸ G. L. Dakovski,⁹ S. Song,⁴ J. M. Glowina,⁴ S. Nelson,⁴ K. W. Kim,⁹ Y.-D. Chuang,² Z. Hussain,¹ R. G. Moore,¹ T. P. Devereaux,¹ W.-S. Lee,¹ P. S. Kirchmann,¹ Z.-X. Shen,^{1,2,1}

The interactions that take place at the emergence of superconductivity in iron-based materials remain a subject of debate. It has been suggested that electron-electron correlations enhance electron-phonon coupling in iron selenide (FeSe) and related pnictides, but direct experimental verification has been lacking. Here we show that the electron-phonon coupling strength in FeSe can be quantified by combining two time-domain experiments with a pump-probe spectroscopy setup. The pump pulse excites the sample, which sends the light-induced femtosecond coherent lattice motion at a single phonon frequency, and photoemission monitors the subsequent coherent changes in the electronic band structure. Comparison with theory reveals a strong enhancement of the coupling strength in FeSe owing to correlation effects. Given that the electron-phonon coupling interactions are the primary responsible for superconductivity in FeSe, our results suggest a cooperative interplay between electron-electron and electron-phonon interactions.

Many of the properties of complex materials, such as the iron-based pricipites and chalcogenides (1), arise from a coupling of charge, orbital, spin, and lattice degrees of freedom. For example, the cooperative interplay of electron-phonon (EP) and electron-electron interactions has been suspected to play an important role in unconventional superconductors (2–4), although the physics beyond the canonical Bardeen-Cooper-Schrieffer theory (5). Although the EP coupling strength can be inferred from various spectroscopies (7, 8), these techniques rely on nontrivial assumptions and modeling. Ultrafast techniques, especially femtosecond time- and angle-resolved photoemission spectroscopy (trARPES) (9) and time-resolved

x-ray diffraction (trXRD) (10), bolstered by the advent of x-ray free-electron lasers (11), now open a window of opportunity for direct measurements of the EP coupling strength with sufficient precision to quantitatively test theories. We combined these two techniques to link electronic and lattice degrees of freedom and determine the EP coupling strength directly and purely from experiments.

The EP coupling strength can be quantified by the deformation potential, defined as the ratio of a band energy shift to the corresponding atomic displacement (12). Experimentally, atoms can be displaced by initiating a coherent phonon mode through photoexcitation of the electrons (13). The light-induced coherent dynamics of the

We report an orbital-resolved coherent lock-in measurement of FeSe that allows us to quantifi-

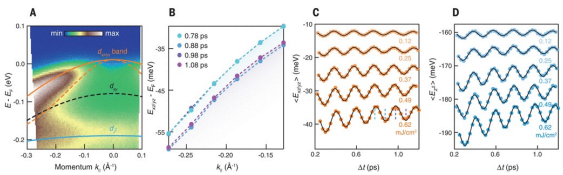


Fig. 2. Coherent electron dynamics. (A) Equilibrium photoemission spectrum at $T = 20$ K along the Γ -X direction. Electronic band dispersions calculated by DFT are overlaid (renormalized by a factor of 3). Dominant features correspond to one of the d_{xy} bands (orange) and the d_{yz} band (blue). Dashed lines indicate unresolved bands, and solid lines indicate detected bands. (B) Photoreduced shift of the d_{xy} band at four delays, corresponding to extrema of the coherent oscillations [denoted by vertical dashed lines in (C)]. (C and D) Momentum-averaged energy shifts of the d_{xy} and d_{yz} bands, respectively. Solid black lines indicate fits of the data. Traces in (C) and (D) are offset for clarity.

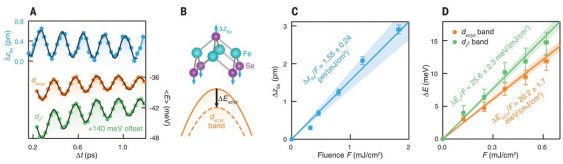


Fig. 3. Coherent lock-in at the A_{1g} frequency. (A) Oscillations of the selenium displacement Δz_{Se} (blue) and the momentum-averaged energy shift (ΔE_{avg}) (orange and green). tRXRD and trARPES data were measured with $F = 0.46$ and $0.37 \mu\text{J}/\text{cm}^2$, respectively. Black lines indicate fits of an exponentially decaying cosine with a polynomial background to extract the peak-to-peak oscillation amplitudes Δz_{Se} and ΔE_{avg} at time zero. (B) Schematic of the A_{1g} phonon mode (top), which periodically modulates the electronic band energies (bottom). (C and D) Lattice and band oscillation amplitudes as a function of the incident pump fluence. Solid lines indicate linear fits. Error bars in (C) and (D) denote statistical uncertainties, whereas the shaded areas represent systematic fluence uncertainties (supplementary text). The error of the fitted slopes accounts for both statistical and systematic uncertainties.

the EP coupling and assess the importance of electron correlations. Using a combination of tRXRD and trARPES, we detect lattice displacements at the subpicometer level and band shifts at the millielectron volt level. Figure 1A is a schematic of the experiment, in which a bulk-like FeSe film (60 unit cells thick) grown on SrTiO_3 is photoexcited by an ultrashort 1.5-eV infrared (IR) pump pulse. For tRXRD, an 8.7-keV hard x-ray pulse tracks the photoinduced lattice dynamics at a variable time delay Δt for trARPES, a 6-eV ultraviolet (UV) pulse records the band energy dynamics (25). Benefiting from the single-mode response in FeSe, we lock-in to the coherent A_{1g} optical phonon (26), which corresponds to a periodic variation of the anion height (Fig. 1B, left inset) that has been shown to sensitively influence the electronic band structure (9, 27), superconductivity (23), and antiferromagnetism (10, 28, 29) of iron-based materials.

Figure 1B shows the (004) Bragg peak intensity of the FeSe film measured by tRXRD upon photoexcitation ($\Delta t > 0$), the diffracted intensity is periodically modulated owing to the collective displacement of the selenium atoms. After subtracting a smoothed incoherent background, the coherent signal is well fit with an exponentially decaying cosine (Fig. 1C). These data and the corresponding Fourier transforms (Fig. 1B, right inset) demonstrate the cleanliness of the coherent response and exemplify the precision of our measurement, which allows resolution of a hand-cueing of the A_{1g} mode by 0.04 ± 0.003 THz with decreasing temperature. Figure 1D shows that the coherent oscillation amplitude increases with increasing pump fluence, whereas the A_{1g} frequency does not noticeably change. The intensity change observed in tRXRD is directly related to the coherent displacement $\delta z_{Se}(t)$ of the selenium atoms by a structure factor calculation

(28) and supplementary text) based on the symmetry of the A_{1g} phonon (Fig. 1E). We use exponentially decaying cosine fits with a linear background to extract the peak-to-peak amplitude Δz_{Se} at time zero. To measure the impact of the coherent A_{1g} phonon on the electronic band structure, we performed trARPES experiments. Photoemission spectra near the Brillouin zone center contain two prominent spectral features (Fig. 2A): (i) a hole-like band, which disperses between energies $E - E_F = 0$ and -100 meV, and (ii) a flat band located at $E - E_F \approx -200$ meV (E_F denotes the Fermi level). High-resolution equilibrium ARPES studies (29, 20) have determined the orbital characters of the electronic bands near E_F by using photon polarization selection rules. Comparison with these studies shows that the first and second bands are of dominant d_{xy} and d_{yz} orbital character, respectively. Electronic

Table 1. Comparison of experiment and theory. Shown are selenium height z_{Se} , A_{Se} phonon frequency ω_{Se} , and A_{Se} deformation potentials $\Delta E_{e\text{-}ph}/\Delta z_{Se}$ and $\Delta E_{e\text{-}ph}/\Delta z_{Se}$ obtained from experiments, canonical DFT calculations, and DFT+DMFT by Mandal *et al.* (5); for $\Delta E_{e\text{-}ph}/\Delta z_{Se}$, the band-average (maximum) values are displayed. The experimental value for z_{Se} is taken from Margadonna *et al.* (30), whereas the deformation potentials are obtained by combining the data shown in Fig. 3, C and D, and applying corrections for spatial integration over pump and probe profiles and effective energy densities (supplementary text). The error of the deformation potentials includes systematic and statistical uncertainties. DFT deformation potentials account for an empirical renormalization factor of 3, and the errors reflect the uncertainty of the renormalization determined from ARPES. Theoretical values for ω_{Se} are deduced from quadratic fits to the relative total energy.

	Experiment	DFT+DMFT (5)	DFT
z_{Se} (reciprocal lattice units)	0.2693	0.27	0.2456
ω_{Se} (terahertz)	5.30 ± 0.05	5.7	6.5 ± 0.3
$\Delta E_{e\text{-}ph}/\Delta z_{Se}$ (millielectron volts per picometer)	-13.0 ± 2.5	-10.3 (-13.4)	-1.6 ± 0.2
$\Delta E_{e\text{-}ph}/\Delta z_{Se}$ (millielectron volts per picometer)	-16.5 ± 3.2	No data	-8.5 ± 0.9

band dispersions calculated by density functional theory (DFT) are overlaid in Fig. 2A with an overall renormalization factor of 3, yielding good agreement with both the d_{xy} and d_{yz} bands. Dashed lines denote bands that do not appear in trARPES, likely because of unfavorable photoemission matrix elements and the limited energy resolution.

The peak energies of the d_{xy} and d_{yz} bands are estimated by fitting two Gaussians to constant-momentum cuts of the spectra (supplementary text). Figure 2B shows the d_{xy} band dispersions at an incident fluence $F = 0.62 \text{ mJ/cm}^2$ and four representative delay times. At all moments, the band energy oscillates with the A_{Se} frequency $f = 5.26 \pm 0.02 \text{ THz}$. The extracted oscillation amplitudes exhibit a momentum k_1 dependence of up to 20% between $k_1 = -0.22$ and -0.13 \AA^{-1} , yet this is comparable in magnitude to the overall uncertainties (supplementary text). Therefore, we average the energy dynamics within this momentum range and display the averaged dynamics for the d_{xy} and d_{yz} bands in Fig. 2, C and D, respectively. We use exponentially decaying cosine fits with a quadratic background to extract the peak-to-peak amplitudes ΔE at time zero.

Figure 3A compares the selenium displacement $\delta z_{Se}(t)$ extracted from trXRD with the energy dynamics of the two electronic bands ($E_{e\text{-}ph}(t)$ and $E_{e\text{-}ph}(t)$) from trARPES. Time zero is independently determined in the two experiments, each yielding an uncertainty of $\sim 20 \text{ fs}$. Within this accuracy, the lattice and electronic oscillations are synchronous: Both bands shift toward lower energy as the selenium atoms move away from the Fe planes (Fig. 3B). This correspondence is the same as that derived for the related compound BaFe_2As_2 (29).

The A_{Se} deformation potential near the Brillouin zone center is quantified by linear fitting of the fluence-dependent amplitudes ΔE_{Se} and $\Delta E_{e\text{-}ph}/\Delta z_{Se}$ shown in Fig. 3, C and D, respectively. We correct for the amplitude reduction caused by the finite time resolutions (supplementary text). Furthermore, for the calculation of the deformation potentials, we include factors to account for the

fluence averaging owing to finite pump and probe beam profiles, as well as for the effective excitation densities per FeSe layer, as determined by the pump and probe penetration depths (supplementary text). The fluence dependences indicate that both the trXRD and trARPES experiments sample a linear response, confirming that the coherent signal remains representative of the ground state. The coherent lock-in approach directly yields deformation potentials of $\Delta E_{e\text{-}ph}/\Delta z_{Se} = -13.0 \pm 2.5$ and $E_{e\text{-}ph}/\Delta z_{Se} = -16.5 \pm 3.2 \text{ meV/pm}$.

The extracted EP deformation potentials allow a comparison with different theoretical approaches. Table 1 shows that canonical DFT, calculated in a nonmagnetic state, underestimates the selenium height and overestimates the A_{Se} frequency. Moreover, the theoretical d_{xy} deformation potential is one order of magnitude smaller than in the experiment. In contrast, the calculated deformation potential of the d_{yz} band is comparable to the experimental value within a factor of 3. The failure of DFT to reproduce these basic properties of FeSe (5, 15, 30) exemplifies the substantial effect of electron correlations on the EP coupling.

These properties can be quantitatively reproduced by using self-consistent DFT+DMFT dynamical mean field theory (DFT+DMFT) to incorporate electron-electron correlation effects (5, 16). For FeSe, this approach (5) yields the correct band structure and selenium height, leading to a softer A_{Se} mode, consistent with experiments (Table 1). In particular, Mandal *et al.* (5) reported a band-averaged (maximum) A_{Se} deformation potential of $(\Delta E_{e\text{-}ph}/\Delta z_{Se}) = 10.3 \text{ meV/pm}$ (3.4 meV/pm) for the d_{xy} band—in agreement with our experimental value.

Our results differ from previous work (10) on BaFe_2As_2 , which reported that the A_{Se} deformation potential obtained from DFT agrees adequately with experiments. This discrepancy may be associated with the non-orbital-resolved nature of the comparison (5, 10) and differences in the level of electron correlations in the two compounds (16). In contrast, our orbital-resolved

lock-in experiment on FeSe establishes a clear case of substantially enhanced EP coupling in the presence of strong correlations.

The important role of correlation-enhanced EP coupling is not universally accepted; most earlier work on iron-based superconductors was focused on spin fluctuations without acknowledging the role of the EP coupling (14–17, 22). Moreover, a direct experimental confirmation of the enhanced EP coupling strength has been lacking: phonon spectroscopies, such as Raman (15) and neutron scattering (16, 27), lack orbital resolution, whereas photoemission (7, 18, 20, 24) and tunneling (8) spectroscopy do not resolve phonons directly. Our method bridges this gap and measures all relevant degrees of freedom directly, allowing us to test theories predicting the effect of correlations on the EP coupling.

In particular, FeSe exhibits a substantial and nontrivial increase in critical temperature T_c from 8 to 37 K by application of pressure (21–23), which matches the pressure dependence of the EP deformation potential derived from DFT+DMFT (5), emphasizing that correlation effects have a strong impact on superconductivity in FeSe. Moreover, the observation of a much-enhanced out-of-plane A_{Se} mode coupling, compared with DFT calculations (Table 1), suggests a small-momentum-transfer EP coupling, consistent with theoretical results for local EP interactions (5). Such a forward-scattering EP coupling likely interferes constructively with other electronic pairing channels (24), thereby providing a pathway toward superconducting states in which EP and electron-electron interactions act in concert.

The coherent lock-in approach establishes an experimental paradigm for precision measurements of fundamental physical quantities, such as the EP deformation potential, by only relying on a linear, coherent response. It provides a purely experimental and model-free technique that simultaneously yields complete information in time, space, momentum, and energy with high sensitivity. Beyond the immediate implication that the “renormalized” EP coupling strength in iron-based materials is considerably larger than anticipated by conventional theories, this approach also opens the way for unbiased tests of emergent phenomena in other controversial, correlated materials.

REFERENCES AND NOTES

1. D. C. Johnston, *Adv. Phys.* **50**, 83–161 (2005).
2. G. S. Bochi, G. G. Gomonov, *Phys. Rev. Lett.* **92**, 164803 (2004).
3. S. Ishizuka, N. Nagata, *Phys. Rev. Lett.* **93**, 036402 (2004).
4. T. P. Yu, A. Kallings, C. Kallier, *Phys. Rev. B* **70**, 220502 (2004).
5. Mandal, R. E. Cohen, Y. Hase, *Phys. Rev. B* **88**, 220502 (2013).
6. J. Bardeen, L. N. Cooper, J. P. Schrieffer, *Phys. Rev.* **108**, 1175–1204 (1967).
7. A. A. Koryukov *et al.*, *Phys. Rev. B* **83**, 134513 (2011).
8. S. Shimada, N. Tsutsui, J. P. Fother, R. W. de Wette, *Physica C* **298**, 195–202 (1998).
9. L. Yang *et al.*, *Phys. Rev. Lett.* **102**, 207001 (2004).
10. L. Yang *et al.*, *Phys. Rev. Lett.* **104**, 057002 (2005).
11. C. Doherty *et al.*, *Rev. Mod. Phys.* **84**, 1057 (2012).
12. G. Grimvall, *The Electron-Phonon Interaction in Metals* (North-Holland Publishing Company, 1981).

RESEARCH | REPORTS

13. H. J. Zenger et al., *Phys. Rev. B* **45**, 768–778 (1992).

14. Z. P. Yin, K. Haule, G. Kotliar, *Nat. Mater.* **10**, 932–935 (2011).

15. V. Gantsevich et al., *Phys. Rev. B* **87**, 144508 (2013).

16. M. C. Bain, R. A. Evers, S. J. Sedlitz, S. J. Clarke, A. T. Boothroyd, *Phys. Rev. B* **91**, 180501(R) (2015).

17. Q. Wang et al., *Nat. Mater.* **15**, 105–109 (2016).

18. T. M. McQueen et al., *Phys. Rev. Lett.* **103**, 057002 (2009).

19. M. D. Watson et al., *Phys. Rev. B* **88**, 155006 (2013).

20. A. Tassi et al., *Phys. Rev. Lett.* **104**, 097002 (2010).

21. S. Moshkalev et al., *Nat. Mater.* **8**, 633–633 (2009).

22. T. Imai, K. Akita, T. Li, T. M. McQueen, R. J. Cava, *Phys. Rev. Lett.* **102**, 177005 (2009).

23. S. Singh et al., *Phys. Rev. B* **80**, 064506 (2009).

24. J. J. Lee et al., *Nature* **515**, 245–248 (2014).

25. Materials and methods are available in supplementary materials.

26. S. Yang et al., *Nat. Mater.* **15**, 4350–4354 (2016).

27. I. Augé et al., *J. Phys. Condens. Matter* **29**, 094003 (2017).

28. A. W. Kim et al., *Nat. Mater.* **11**, 497–501 (2012).

29. S. Gerber et al., *Nat. Commun.* **6**, 7337 (2015).

30. S. Magalhães et al., *Chem. Commun.* **2008**, 5607–5609 (2008).

ACKNOWLEDGMENTS

Use of the LCLS, SLAC National Accelerator Laboratory, is supported by the U.S. Department of Energy (DOE), Office of Science, Office of Basic Energy Sciences (BES) under contract DE-AC02-76BP0085. S.B., S.A.T., H.S., J.A.S., S.R., J.L.L., T.L., B.M., C.L., A.G., Y.L., D.L., L.C., W.L., R.M., T.P.D., W.S.L., P.S.K., and Z.X.S. were supported by the DOE-BES Division of Materials Sciences and Engineering under contract DE-AC02-76BP0085 (the Stanford Institute for Materials and Energy Sciences). The authors gratefully acknowledge technical assistance at LCLS by D. Stefanescu and R. Faltich, S.G. and O.L. acknowledge partial support by the Swiss National Science Foundation under fellowships P12ZP2_148737 and P30QP2_151338, respectively. S.L.S. acknowledges support by the Stanford Graduate Fellowship. H.S. acknowledges support from the Fulbright Scholar Program. A.G. acknowledges support by the National Defense Science and

Engineering Graduate Fellowship Program. K.W.K. was supported by the Basic Science Research Program through the National Research Foundation of Korea, funded by the Ministry of Science, ICT and Future Planning (NRF-2015R1A5A1A01006000). Y.-S.C. and Z.H. were supported by the Director, Office of Science, BES, of the U.S. DOE under contract DE-AC02-05OR21424. Raw data from the time-resolved x-ray scattering experiment are kept at the LCLS. Time-resolved photoemission raw data are kept at the X-ray Laboratory of Stanford University.

SUPPLEMENTARY MATERIALS

www.sciencemag.org/content/357/6346/73/suppl/DC1

Materials and Methods

Supplementary Text

Fig. S1 to S12

Table S1

References (28–44)

27 September 2016; accepted 3 May 2017

10.1126/science.1254996

SUPERCONDUCTIVITY

Discovery of orbital-selective Cooper pairing in FeSe

P. O. Sprau,^{1,2,*} A. Kostin,^{1,3,*} A. Kreisel,^{4,6,*} A. E. Böhm,⁴ V. Taufour,^{1,†} P. C. Canfield,^{4,6} S. Mukherjee,^{1,‡} P. J. Hirschfeld,⁴ B. M. Andersen,⁷ J. C. Séamus Davis^{1,3,8,9,10}

The superconductor iron selenide (FeSe) is of intense interest owing to its unusual nonmagnetic nematic state and potential for high-temperature superconductivity. But its Cooper pairing mechanism has not been determined. We used Bogoliubov quasiparticle interference imaging to determine the Fermi surface geometry of the electronic bands surrounding the $\Gamma = (0, 0)$ and $X = (\pi/a_{\text{FeSe}}, 0)$ points of FeSe and to measure the corresponding superconducting energy gaps. We show that both gaps are extremely anisotropic but nonetheless that they exhibit gap maxima oriented orthogonally in momentum space. Moreover, by implementing a novel technique, we demonstrate that these gaps have opposite sign with respect to each other. This complex gap configuration reveals the existence of orbital-selective Cooper pairing that, in FeSe, is based preferentially on electrons from the d_{xy} orbitals of the iron atoms.

The high-temperature superconductivity in iron-based superconductors is typically most robust where coexisting antiferromagnetic and nematic ordered states are suppressed by doping or pressure (1–5). However, FeSe appears to be distinctive for several reasons: (i) Although strongly nematic, it does not form an ordered magnetic state and is instead hypothesized to be a quantum paramagnet (4–6); (ii) It exhibits evidence for orbital selectivity (7, 8) of band structure characteristics (9–22); and (iii) a monolayer of FeSe grown on a SrTiO_3 substrate has the highest critical temperature T_c of all iron-based superconductors (23–26). It is therefore essential to understand the electronic structure and superconductivity of FeSe at a microscopic level; however, the Cooper pairing mechanism of FeSe has thus far been unknown. A quantitative determination of the momentum-space (k -space) structure and relative sign of the superconducting energy gaps $\Delta_i(k)$ (in each electronic band $E_i(k)$) is necessary to identify this mechanism. So far, this has not been achieved because of the in-

finite Fermi surface pockets, as well as the highly anisotropic $\Delta_i(k)$ requiring an energy resolution $\delta E < 100 \mu\text{eV}$. In this work, we used subkelvin Bogoliubov quasiparticle interference (BQPI) imaging (17–19), an established technique for high-precision multiband $\Delta_i(k)$ determination (20–22), to measure the detailed structure of the energy gaps in FeSe. In the orthorhombic phase below the structural transition temperature $T_S \approx 90 \text{ K}$, FeSe has a crystal unit cell with conventional lattice parameters $a = 5.31 \text{ \AA}$, $b = 5.23 \text{ \AA}$, and $c = 5.48 \text{ \AA}$. We parameterize the Fe plane of the same lattice by using the two inequivalent Fe-Fe distances $a_{\text{Fe}} = 2.665 \text{ \AA}$ and $b_{\text{Fe}} = 2.655 \text{ \AA}$ in the orthorhombic, nematic phase (Fig. 1A and section I of (23)); we define the x axis (y axis) to always be parallel to the orthorhombic a_{Fe} axis (b_{Fe} axis), so that our x - y coordinate system rotates when a twin boundary is crossed. The FeSe Fermi surface is postulated to consist of three bands— α , ϵ , and δ (shown for $k_y = 0$ in Fig. 1B)—and may be parameterized accurately using a tight-binding

model (24, 25) that is fit simultaneously to several types of experimental observations (sections I and III of (23)). Surrounding the $\Gamma = (0, 0)$ point is an ellipsoidal hole-like α -band, whose Fermi surface $k_F(\Gamma = 0)$ has its major axis aligned to the orthorhombic b_{Fe} axis; surrounding the $X = (\pi/a_{\text{Fe}}, 0)$ point is the electron-like ϵ -band whose “bowtie” Fermi surface $k_F(X = 0)$ has its major axis aligned to the orthorhombic a_{Fe} axis. At the $Y = (0, \pi/b_{\text{Fe}})$ point, a δ -band Fermi surface should also exist if its quasiparticles are coherent, but it has not been detectable by spectroscopic techniques. In this picture, the d_{xy} orbital content of the α -band Fermi surface has its maximum value along the x axis (green in Fig. 1B), whereas its d_{xz} orbital content peaks along the y axis (red in Fig. 1B) (25). Conversely, the d_{xy} orbital content of the ϵ -band Fermi surface is maximum along the y axis (green in Fig. 1B), and its d_{xz} orbital content reaches its highest point along the x axis (blue in Fig. 1B) (24–26) and section II of (23). These α -band and ϵ -band Fermi surface pockets (Fig. 1B) exhibit maximal simultaneous consistency with Fermi surface geometry from angle-resolved photoemission spectroscopy (ARPES) (26, 27), quantum oscillations (28, 29), and our BQPI imaging, as discussed below and in section III of (23).

¹Laboratory of Atomic and Solid State Physics, Department of Physics, Cornell University, Ithaca, NY 14853, USA
²Condensed Matter Physics and Materials Science Department, Brookhaven National Laboratory, Upton, NY 11973, USA; Nevis Laboratories, University of Copenhagen, Juliane Maries Vej 30, DK-2300 Copenhagen, Denmark
³Institut für Theoretische Physik, Universität Leipzig, D-04023 Leipzig, Germany
⁴Yonsei University, Yonsei University, Seoul, Korea
⁵Department of Physics and Astronomy, University of Colorado, Boulder, CO 80509, USA
⁶Department of Physics, University of Illinois at Urbana-Champaign, Urbana, IL 61801, USA
⁷Department of Physics, University of Maryland, College Park, MD 20742, USA
⁸Department of Physics, University of California, Davis, CA 95616, USA
⁹Department of Physics, Indian Institute of Technology Madras, Chennai 600036, India
¹⁰Corresponding author. Email: jsamu@cornell.edu

SCIENCE sciencemag.org 7 JULY 2017 • VOL. 357 ISSUE 6346 75